Chalcogenide Letters Vol. 18, No. 10, October 2021, p. 607 - 615

Antimony-doped lead oxide nanoparticles synthesized via using chemical precipitation and annealing treatments: structural and optical properties

K. Srichai, C. Krataitong, A. Tubtimtae*
Department of Physics, Faculty of Liberal Arts and Science, Kasetsart University Kamphaeng Saen Campus, Nakhon Pathom 73140, Thailand

Lead antimony oxide nanoparticles ($Pb_{1-x}Sb_xO$ NPs) were synthesized by chemical precipitation and annealing treatments. The structural and optical properties of undoped and various Sb^{3+}-doped PbO NPs were investigated. The tetragonal phase of α-PbO was found for both before and after various Sb^{3+} doping. The lattice parameters decreased for the 1.0 – 5.0 wt% Sb^{3+} doping, which indicated the increase of internal defects, but tends to an amorphization with exceeding 5.0 wt%. The overall band gap (E_g) values after Sb^{3+} doping (1.07–1.76 eV) are lower than undoped PbO (2.35 eV). These findings indicate a promising material for window layer fabrication and an absorber material for solar cell applications.

(Received June 20, 2021; Accepted October 12, 2021)

Keywords: PbO nanoparticle, Sb^{3+} doping, Chemical precipitation and annealing treatments, Crystal structure, Optical materials and properties

1. Introduction

Recently, metal chalcogenide thin film and semiconducting oxide nanoparticles (NPs) or nanostructures have attracted much attention and significant in many technological applications such as photodetector, laser, light emitting diodes, liquid crystal displays, touch screen, pseudocapacitor, and photovoltaic devices [1-5]. Beside the research of a metal oxide material, In_2O_3 nanostructures doped by iron (Fe) synthesized via a freeze-drying process has been previously reported [6], one of semiconducting oxide nanoparticle that we interested is lead oxide (PbO), due to previously demonstrated as a photoactive layer in schottky type photovoltaic devices [7].

As we know, nanostructured PbO has two kinds, which performs different optical and structural properties. α-PbO has a band gap of 1.9 eV, which is commonly applied in photovoltaic application [8] and β-PbO with a band gap of 2.8 eV was used as surface modifiers [9]. To seek more attention on the physical properties of material, various dopants and concentrations in the PbO films can be tuned its crystallinity and energy band gap such as Mn, Co, Ce, Ni, Zn [10-14]. These 3*d* elements acted as excellent dopants for the synthesis of pure and homogeneous PbO NPs with high surface area because of its low decomposition temperature [10]. Meanwhile, undoped and doped PbO NPs have been synthesized by different methods to study the surface morphologies, structural, and optical properties such as simple ultrasonic spray pyrolysis [10], electro-deposition [11], sol-gel [15], and chemical bath deposition [16]. Nevertheless, among these 3*d* element dopants and synthesis methods, we are firstly synthesized the PbO NPs doped with various antimony (Sb) concentrations via using precipitation and annealing treatments to form the $Pb_{1-x}Sb_xO$ NPs. We have also investigated the effect of the Sb doping in the PbO NPs, which was playing an important role in tuning of structural and optical characteristics for potential optoelectronics devices such as UV sensors, diode lasers, photovoltaic, and solar cells. The crystallinity, structural characteristics performed using transmission electron microscopy (TEM), and X-ray powder diffraction (XRD). Vibration modes of chemical compositions were observed by infrared spectroscopy (FTIR). The optical properties were conducted by UV-Vis spectroscopy.

* Corresponding author: tubtimtae@gmail.com
https://doi.org/10.15251/CL.2021.1810.607

It can be seen that this demonstration correlates the effect of Sb doping concentration to particle size, and energy band gap of the PbO NPs.

2. Experimental section

$Pb_{1-x}Sb_xO$ NPs were synthesized by dissolved 0.1 M lead acetate trihydrate ($(CH_3COO)_2Pb{\cdot}3H_2O$) and 0.1 M sodium hydroxide (NaOH) in deionized (DI) water with various concentrations for Sb doping of 0.0, 1.0, 3.0, 5.0, 7.0, and 9.0 wt% (x = 0.00, 0.01, 0.03, 0.05, 0.07, and 0.09) and vigorously stirred under the temperature of 70 °C for one hour until the white homogeneous solutions were performed. Afterward, the solutions were transferred into a glass plate for thermal evaporation under the temperature of 130 °C for three hours to form the white precipitation. Then, the precipitation in a glass plate was annealed in an oven at 450 °C for four hours. The dark-red precipitation was scratched out and grounded for 60 min until it became NPs, as shown in Fig. 1. Structural characteristics of $Pb_{1-x}Sb_xO$ NPs were performed using XRD (BRUKER, D2 Phaser) with Cu-Kα radiation (λ = 1.5406 Å), operating at 30 kV and 10 mA over a 2θ range of 10° to 80° (interval of 0.02°). The crystallite sizes were calculated by the Williamson-Hall (W-H) method using the seven intense diffraction peaks. The particle sizes and shapes were observed by TEM (FEI–Tecnai G^2 S-TWIN), operating at 200 kV. FTIR spectra were investigated using the KBr pellet procedure from 400 to 4000 cm^{-1} (PerkinElmer Frontier™). Finally, transmittance spectra of $Pb_{1-x}Sb_xO$ NPs in ethanol were displayed via UV-Vis spectroscopy (Thermo Scientific BioMate™ 160) in the 300 – 1100 nm range.

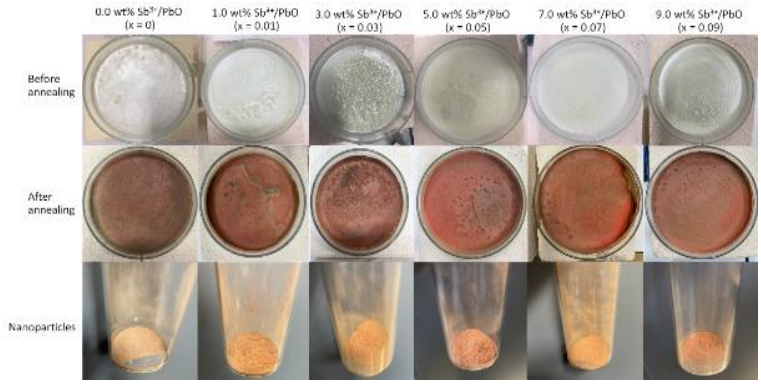

Fig. 1. Sample preparation for before, after annealing and NPs of various Sb^{3+} doping in the PbO NPs.

3. Results and discussion

Fig. 2 shows the X-ray diffractograms of the $Pb_{1-x}Sb_xO$ NPs and the structural parameters are listed in Table 1. The crystallographic patterns confirm the α phase of tetragonal structure for both undoped and Sb^{3+}-doped PbO NPs (JCPDS no. 05-0561) without any secondary phases or impurity in the samples. The clear distinct peaks are assigned at 2θ ≈ 28.60°, 31.80°, 35.70°, 48.60°, 54.70°, 59.20°, and 59.90°, which are corresponding to the (101), (110), (002), (112), (211), (202), and (103), respectively.

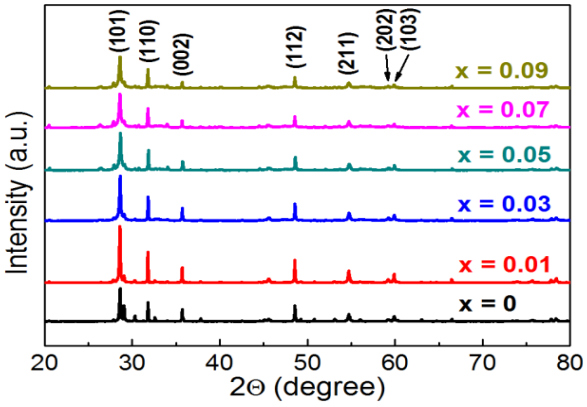

Fig. 2. XRD patterns of the $Pb_{1-x}Sb_xO$ NPs.

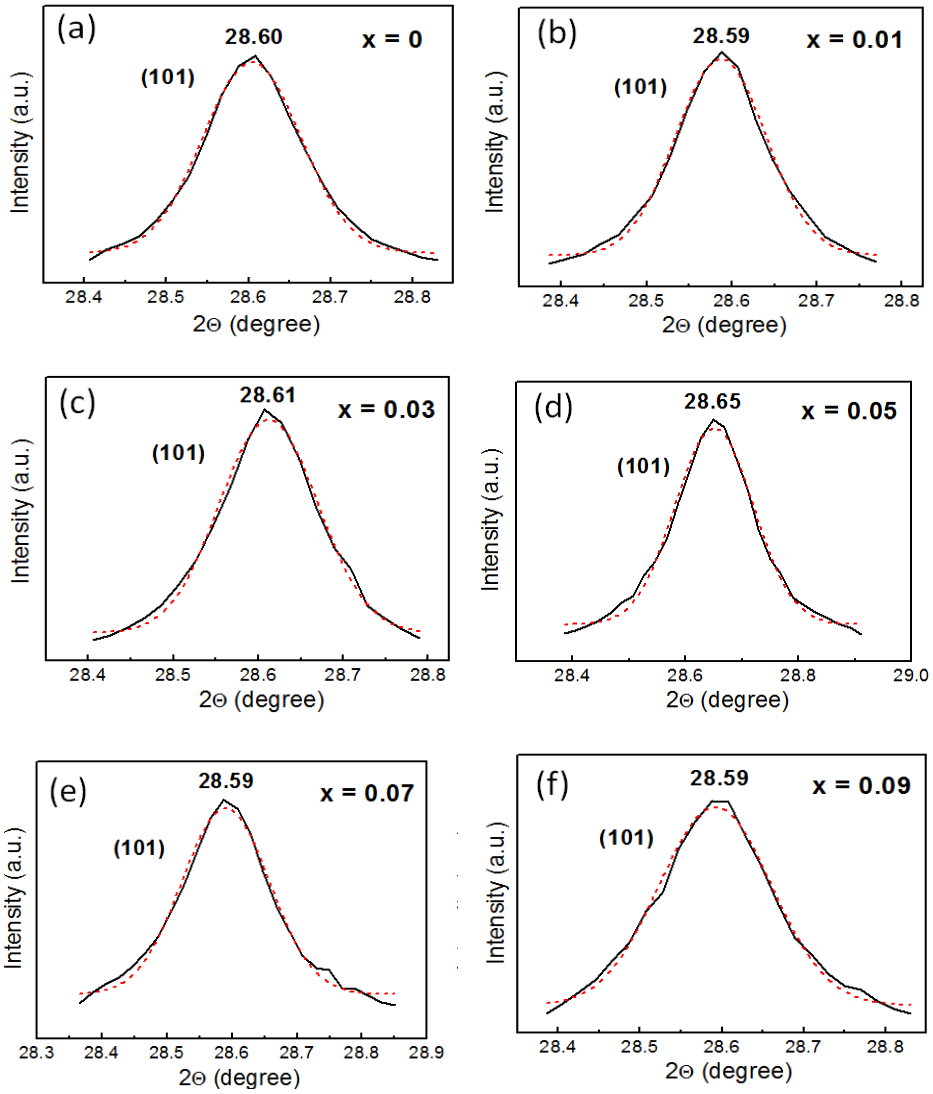

Fig. 3. Enlarged XRD peak for the (101) plane with various Sb^{3+} doping in the PbO NPs.

Fig. 3 shows a highest intensity and a broadening of the (101) peaks with various Sb^{3+} doping concentration (x = 0.01 – 0.09). The d-spacing, $d_{(hkl)}$ can be calculated from the Bragg equation as the relation [17]:

$$d_{hkl} = \frac{n\lambda}{2sin\theta} \quad (1)$$

where, n = 1 for first order diffraction, λ is the wavelength of the X-ray source for Cu-Kα radiation (λ = 1.5406 Å), θ is the Bragg diffraction angle, and h, k, and l are the Miller indices. The lattice parameters (a = b, c) were then calculated from the relation (2) and (3), respectively [18,19]:

$$a = d_{hkl}\sqrt{h^2 + k^2 + l^2} \quad (2)$$

and

$$\frac{1}{d_{hkl}^2} = \frac{4}{3}\left(\frac{h^2+hk+k^2}{a^2}\right) + \frac{l^2}{c^2} \quad (3)$$

In Fig. 4(a), the values decreased for the 1.0 – 5.0 wt% Sb^{3+} doping (x = 0.01 – 0.05), which indicated the increase of internal defects due to the Sb atoms (1.45 Å) are substituted into the Pb atoms (1.80 Å) [20]. This doping interval may attribute to a narrowing of the PbO lattice in the two principal directions (a, c). Then, the a and c values increased with exceeding 5.0 wt% due to a saturation of substitutional sites takes place and the excessive addition of Sb (beyond 9.0 wt%, x = 0.09) leads to the crystallite disorientation, which tends to an amorphization of material. Similar trends were also obtained in the Al-doped ZnO thin films prepared by the reactive chemical spray method [21].

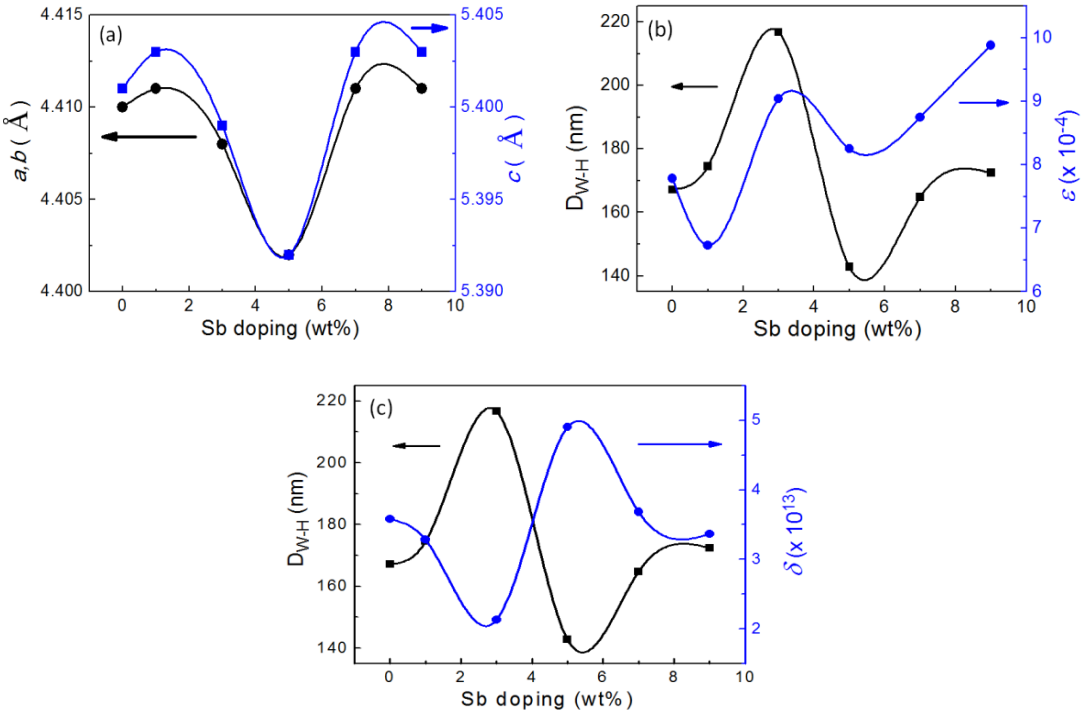

Fig. 4. (a) lattice parameters, (b) crystallite size and strain, and (c) crystallite size and dislocation density.

Furthermore, the crystallite sizes ($D_{W\text{-}H}$) were calculated using the Williamson–Hall (W–H) plot with strain (ε) and dislocation density (δ) induced on the $Pb_{1-x}Sb_xO$ NPs for various Sb^{3+} doping concentrations were respectively calculated by the following equations [22]:

$$\beta_{hkl}cos\theta = \left(\frac{k\lambda}{D_{\text{W-H}}}\right) + 4\varepsilon sin\theta \tag{5}$$

and

$$\delta = \frac{1}{D_{\text{W-H}}^2}, \tag{6}$$

where β_{hkl} is the integral width of peak, K is the shape factor, normally is 0.89. Based on the linear fit by plotting the graph of $\beta_{hkl}\cdot\cos\theta$ vs. $4\sin\theta$ in Fig. 5, the $D_{\text{W-H}}$ was determined from the y-intercept, and the ε was indicated from the slope of the fit. The results were illustrated in Figs. 4(b and c), respectively. The trend of ε values was increased with the $D_{\text{W-H}}$ when Sb^{3+} doping exceeds 1.0 wt% (x = 0.01). While, the opposite trend of δ with the $D_{\text{W-H}}$ was also found. The large change of δ increasing was obtained for Sb^{3+} doping from 3.0 wt% (x = 0.03) to 5.0 wt% (x = 0.05). This also shows the large increase of degradation and defects in the $Pb_{1-x}Sb_xO$ NPs due to this interval of Sb^{3+} doping concentration may enhance sufficient defect diffusion energy to migrant the $Pb_{1-x}Sb_xO$ lattice position and more randomly oriented and distributed crystallites [23].

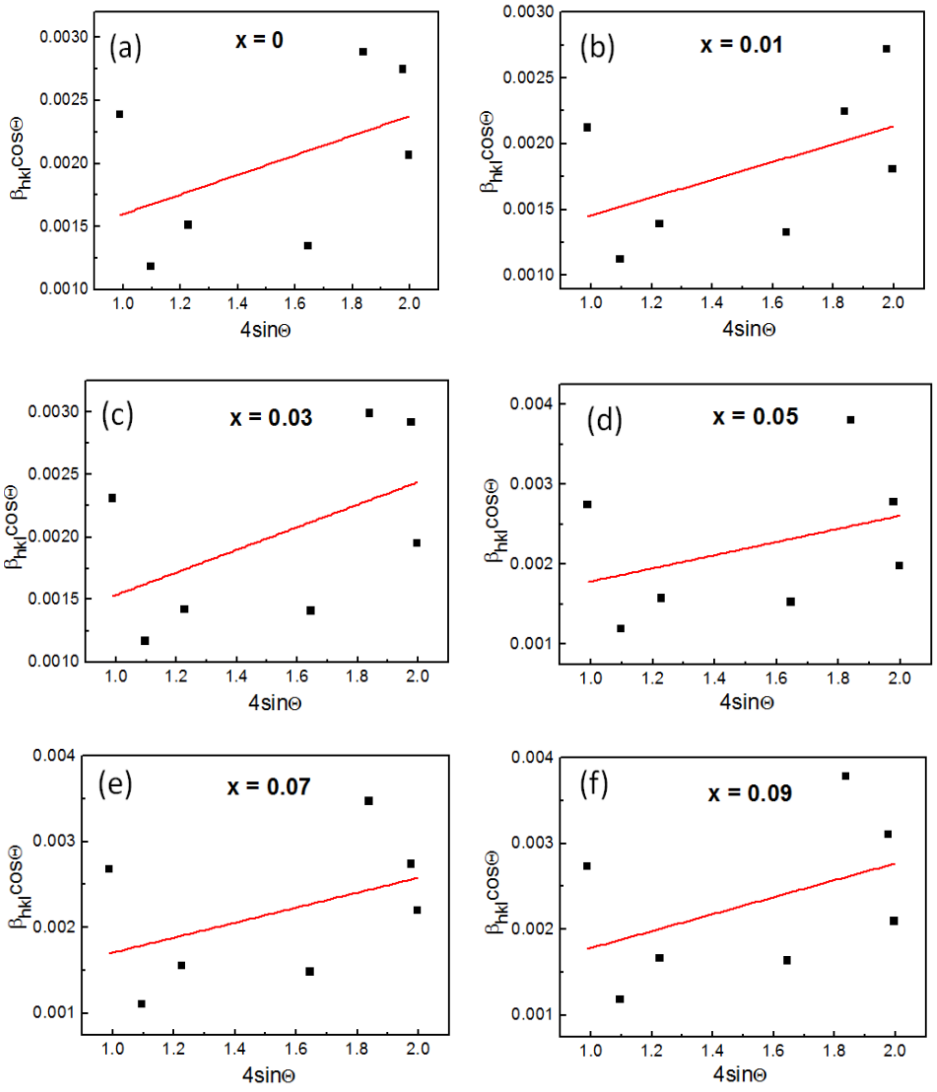

Fig. 5 Williamson-Hall plots for estimating the crystallite size with various Sb^{3+} doping in the PbO NPs.

Table 1. Crystallographic parameters and crystallite size of the $Pb_{1-x}Sb_xO$ NPs.

Sb doping (x)	d-spacing (Å)	$a = b$ (Å)	c (Å)	ε ($\times 10^{-4}$)	$D_{W\text{-}H}$ (nm)	$\langle D \rangle_{TEM}$ (nm)	δ ($\times 10^{13}$)
0.00	3.1182	4.410	5.401	7.783	167.15	169.82 ± 90	3.579
0.01	3.1193	4.411	5.403	6.732	174.56	178.84 ± 80	3.282
0.03	3.1172	4.408	5.399	9.042	216.71	220.75 ± 60	2.129
0.05	3.1129	4.402	5.392	8.251	142.81	144.75 ± 90	4.903
0.07	3.1193	4.411	5.403	8.748	164.76	157.45 ± 110	3.684
0.09	3.1193	4.411	5.403	9.882	172.47	178.20 ± 70	3.362

Figs. 6 (a and c) shows a TEM micrograph for the representative PbO (x = 0.00) and $Pb_{0.07}Sb_{0.03}O$ (x = 0.03) NPs and the histogram shows the particle size distribution in Figs. 6(b and d), respectively. The image reveals that the NPs were formed and aggregated in various shapes in both NPs of x = 0.00 and 0.03. The average particle sizes $\langle D \rangle_{TEM}$ for x = 0.00 and 0.03 were estimated to be 169.82 ± 90 and 220.75 ± 60 nm, respectively. However, the $\langle D \rangle_{TEM}$ of other Sb^{3+} doping condition can also be observed via a TEM micrograph and presented in Table 1. It can be seen that both the crystallite size from the W-H method and particle size from the TEM image are agreed and indicated to as polycrystalline. The FTIR spectra for the $Pb_{1-x}Sb_xO$ NPs are performed in Fig. 7. The broad absorption band at 1425 cm^{-1} arises from the antisymmetric and symmetric stretching vibration of the carboxylic group (C–O). The peak bands at 458, 691, and 878 cm^{-1} are indicated as metal–oxygen (M–O) stretching vibrations [24]. The absence of other peaks may be recognized that the Sb atom was substitutional to the Pb atom in the host PbO lattice, which agreed with the work of A. A. Oliveira et al. [6].

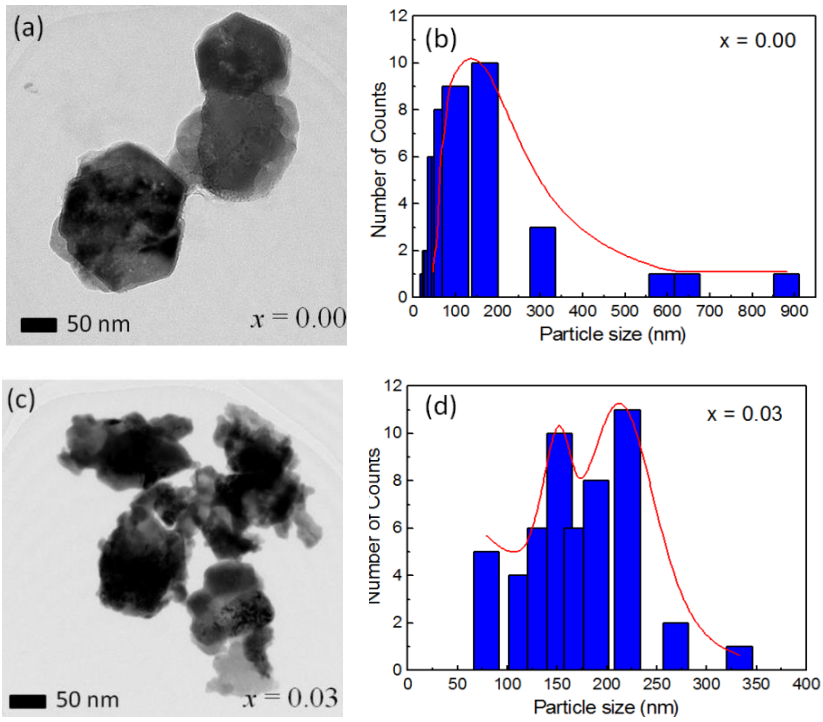

Fig. 6 (a,c) TEM micrograph, (b,d) histogram for particle size distribution for x = 0.00 and 0.03, respectively.

Fig. 8(a) shows the transmittance as a function of wavelength for the $Pb_{1-x}Sb_xO$ NPs. The trend of transmittance decreases from Sb^{3+} doping of x = 0.00 to 0.03 and then fluctuate increasing and decreasing again for x = 0.05 and 0.09, respectively. Consequently, the Tauc's plot and E_g for all Sb^{3+} doping conditions determined by the relation [25]:

$$Ahv = B(hv - E_g)^n \,, \tag{7}$$

where A is an absorbance which was calculated from the transmittance through the relation: $A = -logT(\lambda)$, B is a constant, and n is the index of inter-band transition (i.e., n = 1/2 for direct allowed transitions). The linear extrapolation on the x-axis was shown in Fig. 8(b) and the plot of E_g with various Sb^{3+} doping was illustrated in Fig. 8(c). The E_g for the undoped PbO NPs is 2.35 eV, which is very close to the value in the previous literature for the PbO thin film synthesized by a spray pyrolysis method (E_g = 2.36 eV) [26].

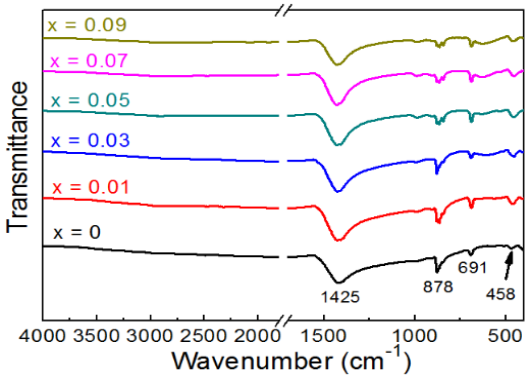

Fig. 7 FTIR spectra of the $Pb_{1-x}Sb_xO$ NPs.

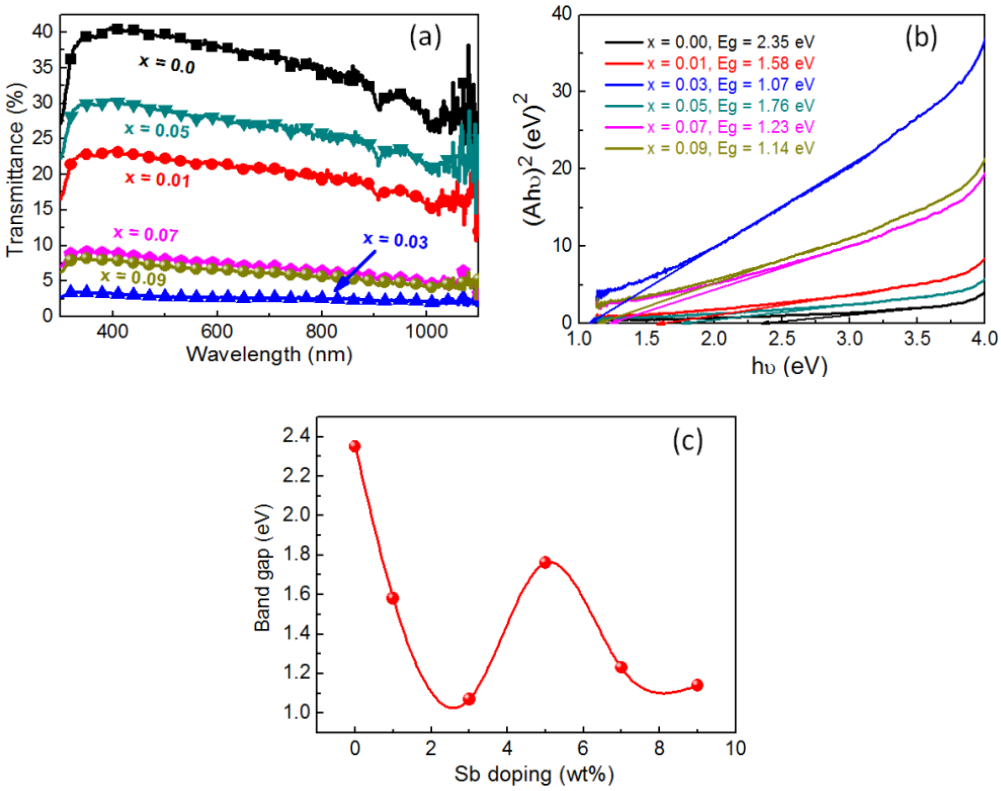

Fig. 8. (a) Transmittance spectra, (b) Tauc's plot, and (c) plot of energy band gap for the $Pb_{1-x}Sb_xO$ NPs.

Furthermore, the doped PbO NPs had decreasing E_g with increasing Sb^{3+} doping to 3.0 wt%. The lowest E_g was found to be 1.07 eV and then increase to 1.76 eV for 5.0 wt% Sb^{3+}

doping. However, the overall E_g values after Sb^{3+} doping are lower than the undoped PbO NPs. Similar to the previous report [6], this attributed the redshift to the host charge carrier-dopant (*sp-d*) exchange interactions between the electron of the host PbO and the 3*d* electron of Sb cations. Thus, the conduction band edge shifts downwards and the valence band edge shifts upwards, leading to a decrease in energy band gap. These findings for the maximum and minimum band gaps for undoped and optimum Sb^{3+} doping can be supported by the explanation of P.U. Asogwa [27]; higher band gap value semiconductors are used as a window layer in fabrication of solar cell and the low band gap values can be potentially applied as an absorber material in solar cell fabrication.

4. Conclusions

$Pb_{1-x}Sb_xO$ NPs were synthesized by chemical precipitation and annealing treatments. The tetragonal α-PbO phase was found for both before and after various Sb^{3+} doping concentrations. The lattice parameters decreased for the 1.0 – 5.0 wt% Sb^{3+} doping, which indicated the increase of internal defects, but tends to an amorphization with exceeding 5.0 wt%. The overall E_g values after Sb^{3+} doping are lower than undoped PbO. These findings indicate a promising material for window layer fabrication and an absorber material for solar cell applications.

Acknowledgments

This research was supported by the Faculty of Liberal Arts and Science, Kasetsart University, Kamphaeng Saen Campus, Thailand.

References

[1] S. H. Babu, S. Kaleemulla, N. M. Rao, C. Krishnamoorthi, J. Magn. Magn. Mater. **416**, 66 (2016).
[2] C. Krataitong, K. Srichai, A. Tubtimtae, Mater. Lett. **285**, 129085 (2021).
[3] P. Boon-on, C. R. Chiang, R. Rajendran, N. Suriyawong, J. B. Shi, M. W. Lee, J. Power Sources **485**, 229324 (2021).
[4] A. Tubtimtae, P. Pluengphon, B. Inceesungvorn, Mater. Lett. **300**, 130140 (2021).
[5] D. Raknual, S. Charoenphon, P. Reunchan, A. Tubtimtae, Electrochim. Acta **389**, 138773 (2021).
[6] A. A. Oliveira, M. I. Valerio-Cuadros, L. F. S. Tupan, V. S. Zanuto, F. F. Ivashita, A. Paesano Jr., Mater. Lett. **250**, 210 (2019).
[7] L. M. Droessler, H. E. Assender, A. A. R. Watt, Mater. Lett. **71**, 51 (2012).
[8] B. Thangaraju, P. Kaliannan, Semicond. Sci. Technol. **15**, 542 (2000).
[9] K. C. Chen, C. W. Wang, Y. I. Lee, H. G. Liu, Eng. Aspects **373**, 124 (2011).
[10] V. N. Suryawanshi, A. S. Varpe, M. D. Deshpande, Thin Solid Films **645**, 87 (2018).
[11] A. B. Velichenko, R. Amadelli, E. A. Baranova, D. V. Girenko, F.I. Danilov, J. Electroanal. Chem. **527**, 56 (2002).
[12] W. Zhang, Y. Xie, J. Gu, S. Ai, J. Wang, K. Yamamoto, L. Jin, Analyst **129**, 229 (2004).
[13] Y. Xia, Q. Dai, J. Chen, J. Electroanal. Chem. **744**, 117 (2015).
[14] M. Azarang, M. Aliahmad, A. G. Shiravizadeh, H. R. Azimi, R. Yousefi, J. Appl. Phys. **124**, 123101 (2018).
[15] M. M. Kashani-Motlagh, M. K. Mahmoudabad, J. Sol-Gel Sci. Technol. **59**, 106 (2011).
[16] D. D. O. Eya, Pac. J. Sci. Technol. **7**, 114 (2006).
[17] W. Y. Zhang, J. G. Zhao, Z. Z. Liu, Z. J. Liu, Z. X. Fu, Appl. Surf. Sci. **256**, 4423 (2010).
[18] A. Jafari-Rad, H. Kafashan, Ceram. Int. **45**, 21413 (2019).
[19] M. Mazhdi, P. H. Khani, Int. J. Nano Dimens. **4**, 233 (2012).

[20] J. C. Slater, J. Chem. Phys. **41**, 3199 (1964).
[21] A. Nakrela, N. Benramdane, A. Bouzidi, Z. Kebbab, M. Medles, C. Mathieu, Results Phys. **6**, 133 (2016).
[22] M. Sathya, K. Pushpanathan, Appl. Surf. Sci. **449**, 346 (2018).
[23] G. Singh, S. B. Shrivastava, D. Jain, S. Pandya, T. Shripathi, V. Ganesan, Bull. Mater. Sci. **33**, 581 (2010).
[24] M. Nafees, M. Ikram, S. Ali, Appl. Nanosci. **7**, 399 (2017).
[25] S. U. Rahayu, M. W. Lee, AIP Conf. Proc. **2221**, 030005 (2020).
[26] M. Suganya, N. Narasimman, J. Srivind, V. S. Nagarethinam, K. Usharani, A. R. Balu, J. Electron. Devices **21**, 1842 (2015).
[27] P. U. Asogwa, Chalcogenide Lett. **8**, 163 (2011).